arXiv:2207.05045v3 [cond-mat.str-el] 19 Dec 2022

Emergence of bond-dependent highly anisotropic magnetic interactions in Sr_4RhO_6: a theoretical study

Shishir Kumar Pandey,[1,2,*] Qiangqiang Gu,[2,3] Yihao Lin,[1] Rajarshi Tiwari,[4] and Ji Feng[1,5]

[1] *International Center for Quantum Materials, School of Physics, Peking University, Beijing 100871, China*
[2] *AI for Science Institute, Beijing, China*
[3] *School of Mathematical Science, Peking University, Beijing 100871, China*
[4] *School of Physics, AMBER and CRANN Institute, Trinity College Dublin, Dublin 2, Ireland*
[5] *Hefei National Laboratory, Hefei 230088, China*

(Dated: December 20, 2022)

The quantum spin liquid states as a natural ground state of the Kitaev model has led to a quest for new materials candidates hosting Kitaev physics. Yet, there are very few material candidates in this category. Using a combination of *ab initio* and model Hamiltonian methods, we propose that Ruddlesden-Popper compound Sr_4RhO_6 belongs to this category. With a tight-binding model and exact diagonalization approach, we show that despite substantial trigonal-like distortion, the electronic and magnetic properties of Sr_4RhO_6 can be well described in terms of pseudo-spin = 1/2 states. Magnetic interactions among pseudo-spins, estimated using the second-order perturbation method are highly bond-dependent anisotropic in nature with two particularly noticeable features, antiferromagnetic Kitaev and Dzyaloshinskii-Moriya interactions. The gaped spin-wave spectra of Sr_4RhO_6 obtained with linear spin-wave theory is consistent with the underlying magnetic frustration. Additional analysis of the role of individual or a particular combination of magnetic interactions reveals that the spin-wave spectra of Sr_4RhO_6 is a combined effect of the highly anisotropic interactions and a relatively simpler minimal model may not be plausible in the current case. The crucial insights about coupling between the local structural features and magnetic properties of Sr_4RhO_6 obtained in this study may be helpful for future studies belonging to this class.

I. Introduction

Orbital and spin angular momentum of an electron are coupled through a relativistic effect called spin-orbit coupling (SOC). Many interesting phenomena such as the anomalous Hall effect, manipulation of spin currents, the emergence of topological properties in weakly correlated systems has been extensively studied [1–3] . However, the strongly correlated materials provide host even richer physics because of the presence of additional interactions such as crystal field splitting ($\Delta^{\rm CF}$) and on-site Hubbard (U), often competing with SOC [4, 5]. This competition gives rise to exotic phenomenon like realization of unconventional superconductivity [6–8], emergence of topological phases [9] and Kitaev physics [10]. Among these examples, Kitaev physics [11] particularly has recently got a lot of attention as a driving mechanism in realization of quantum spin liquid states [12, 13].

The work of Jackeli and Khaliullin [10] accelerated the progress towards the realization of Kitaev physics in real materials. Their proposal was based on magnetic interactions between pseudo-spins on a honeycomb lattice of transition metal ions originating from the interplay of strong electrostatic crystal field (CF) of anions and SOC at transition metal sites. The five degenerate d orbitals of transition metal atom split into triply degenerate t_{2g} and doubly degenerate e_g orbitals due to $\Delta^{\rm CF}$ (see Fig. 1(a)). Energetically lower t_{2g} manifold further splits in the presence of SOC to form the half-filled pseudo-spin $J_{\rm eff} = \frac{1}{2}$ states dominating low energy space of materials. Magnetic interactions between these $J_{\rm eff} = \frac{1}{2}$ pseudo-spin states was proposed to be dominantly Kitaev-type. Cobaltates [14–23], iridates [24–31] and α-$RuCl_3$ [32–36] are some of the examples falling in this category. Recent studies on Ir-based double perovskite compounds have further widen the horizon of Kitaev physics on frustrated fcc lattice formed by magnetic ions with spatially separated octahedral environment [37–41].

These pseudo-spin $J_{\rm eff} =\frac{1}{2}$ doublets are Kramers's doublet which relate to each other by time-reversal symmetry and are degenerate when time-reversal symmetry is preserved. The associated operators, $\boldsymbol{J}_{\rm eff}{}^{\gamma}$, where $\gamma = x$, y, z, thus follow the spin commutation relations. Only in the limits, $\Delta^{\rm CF} \to \infty$ and when the splitting among the t_{2g} manifold due to additional trigonal(tetragonal) distortions $\Delta^{\rm CF}_{\rm tri.}(\Delta^{\rm CF}_{\rm tet.}) \to 0$, a pure $J_{\rm eff} =\frac{1}{2}$ state can be realized.

However, the real materials mentioned above are far from these ideal limits making the situation even more complex. Such complexities are inevitable when a minor change in details of these interactions may have dramatic effects on the macroscopic behavior of the material. For example, in iridates despite the presence of additional $\Delta^{\rm CF}_{\rm tri.}(\Delta^{\rm CF}_{\rm tet.})$ distortions which are responsible for mixing between $J_{\rm eff} =\frac{1}{2}$ and $\frac{3}{2}$ states [27, 31], the large SOC of Ir $5d$ orbitals still allow $J_{\rm eff}= \frac{1}{2}$ description of the magnetic properties. However, same cannot be pre-assumed for a $4d$ transition metal compound where SOC strength is nearly half of its $5d$ counterpart and $\Delta^{\rm CF}_{\rm tri.}(\Delta^{\rm CF}_{\rm tet.})$ distortions of octahedra might be comparable to the SOC

* shishir.kr.pandey@gmail.com

strength. This inhibits any generic rule for behavior prediction of such materials and hence, a case to case study is often required.

The scarcity of 4*d* magnetic compounds with $J_{\rm eff} = \frac{1}{2}$ behavior makes it even more difficult to obtain any comprehensive understanding. To the best of our knowledge, the only example of magnetic material in this category is α-$RuCl_3$ and has been the subject of extensive theoretical and experimental investigations [32–36]. Other 4*d* materials such as Li_2RhO_3, Sr_2RhO_4, and some theoretically predicted Rh and Ir-based fluorides are either nonmagnetic (Li_2RhO_3 shows spin-glass behavior) or paramagnetic in nature [42–44]. In the quest of new Kitaev candidates, Sr_4RhO_6 is another possible example of a 4*d* oxide [45, 46]. Materials like Sr_4RhO_6 and some Ir-based double perovskites [37–41]) with isolated metal-anion octahedra (as shown in Fig. 1(b)) may possess an advantage over materials with edge-shared geometry because the larger spatial separation between the magnetic ions in the former can minimize the direct overlap of *d* orbitals as compared to edge shared geometry. This in turn may result in suppression of additional *undesirable* nearest-neighbor as well as farther neighbor Heisenberg-like isotropic coupling. Sr_4RhO_6 is believed to exhibit ideal cubic octahedral environment on Rh-sites [46] in a centrosymmetric crystal structure. Such a distinctive feature may lead to the realization of *pure* $J_{\rm eff}$ =1/2 states, a feature not realized in any of the previously mentioned Kitaev candidate materials. Despite purportedly having such lucrative features with the possibility of hosting rich physics, it is surprising to find no theoretical study dedicated to this material and hence is the focus of our study in this article.

In this study, using a combination of first-principles calculations and a tight-binding model, we first show that contrary to the earlier belief [46], the Rh-O_6 octahedra in Sr_4RhO_6 is not perfect and the octahedral crystal field at Rh-sites has additional trigonal-like distortions originating from the influence of the extended environment of Sr atoms. Using the exact diagonalization (ED) technique, we show that despite such a distortion, mixing between $J_{\rm eff}$ = 1/2-3/2 states is small and description of low-energy space in terms of $J_{\rm eff} = 1/2$ states is still valid in this material. Magnetic interaction among these pseudo-spins estimated using second-order perturbation theory show highly bond-dependent anisotropic behavior with additional diagonal/off-diagonal terms appearing alongside two particularly noticeable features, antiferromagnetic Kitaev and Dzyaloshinskii-Moriya (DMI) interactions on some of the first nearest-neighbor (1NN) Rh-Rh bonds. We attribute the appearance of DMI to the local inversion symmetry breaking due to the extended environment of Sr^{+2} ions. The second and third nearest-neighbor interactions are found to be negligibly small. The classically optimized magnetic ground state brings an antiferromagnetic configuration which is energetically close to the previously proposed magnetic structure. Spin wave spectra calculated using linear spin-wave theory is found to be gaped throughout the Brillouin zone, consistent with underlying frustrated magnetic frustration. Origin of various features of the spectra is analyzed separately by examining the role of various magnetic interaction terms in the spin Hamiltonian. This analysis establish the fact that the spectra is a combined effort of all these highly anisotropic magnetic interactions and a relatively simpler minimal magnetic model may not be plausible in the current case. Our study provides crucial insights for compounds belonging to this class.

II. Methods

A. *Ab initio* calculations

Density-functional theory calculations have been performed using projector-augmented wave method [47, 48], implemented within Vienna *ab initio* simulation package (VASP) [49]. The Perdew-Burke-Ernzerhof functional [50] is used for the exchange-correlation functional within the GGA formalism. We start with the experimental lattice parameters of trigonal crystal system of Sr_4RhO_6 with centrosymmetric space group $R\bar{3}c$ (No. 167) which are $|\mathbf{a}| = |\mathbf{b}| = 9.740$ Å, $|\mathbf{c}| = 11.840$ Å; $\alpha = \beta = 90^\circ$ and $\gamma = 120^\circ$ [46]. Using plane wave cutoff energy 550 eV, $4 \times 4 \times 2$ Γ-centered *k*-mesh and energy convergence criteria of 10^{-5} eV, we optimize the lattice parameters with experimentally proposed magnetic ground (accommodated within 24 Rh atoms in a $2 \times 2 \times 1$ supercell) considering SOC effect at the self-consistent level. A DFT+U approach employing Liechtenstein [51] scheme with on-site Coulomb interaction U = 2.5 eV and exchange interaction $J_{\rm H}$ = 0.9 eV was used. The values of U and $J_{\rm H}$ parameters are consistent with the previous study [46]. Optimized a and b lattice constants were found to be overestimated by $\sim$ 3.1 % while c remains the same. Since this change in lattice constants is significant, we have used the optimized structure in further calculations.

B. Estimation of electronic parameters

Non spin polarised tight-binding (TB) Hamiltonian ($H_{\rm TB}$) in local axes framework (see Fig. 1(b)) was calculated by projecting onto all the five Rh-*d* orbitals using the Wannierization procedure [52] and is shown in Fig. 2(a). On the two symmetry in-equivalent Rh sites, octahedron are rotated around the C_3-axis which is along crystallographic $\boldsymbol{c}$ axis. We choose the local axes ($\boldsymbol{x}$, $\boldsymbol{y}$, $\boldsymbol{z}$) along oxygen atoms on one of the Rh site obeying $\boldsymbol{c} = \boldsymbol{x} + \boldsymbol{y} + \boldsymbol{z}$ and rotate these axes on the other Rh site by a unitary transformation to obtain the identical form of CF matrix on the two sites. Crystal field matrix on a site i ($\Delta_i^{\rm CF}$) is extracted from the onsite part of $H_{\rm TB}$ obeys crystals C_3 symmetry. To extract the SOC strength (λ),

we fit the *ab inito* band structure, where the SOC was included at the self-consistent level, with $H_{\rm TB}$ after adding the onsite $H_{\rm soc} = \sum_i \lambda \boldsymbol{L}_i \cdot \boldsymbol{s}_i$ term [53]. The fitting is shown in Fig. 2(C) with the inset showing the fitting near the Fermi level. It brings $\lambda = 90$ meV. This vaue is smaller than the considered value for iso-electronic α-$RuCl_3$ ($\lambda = 140$ meV) [36, 54] and a recently estimated value of 175 meV for Rh atom [55]. However, on a later stage, we will show that considering these three values does not bring any qualitative changes in the magnetic interactions and hence, for rest of the discussion in the manuscript we choose $\lambda = 140$ meV. We estimate the Coulomb matrix elements $U_{ijkl}(\omega = 0)$ within the constrained random phase approximation (cRPA). To this end, we neglect the screening effects for all the five Rh d orbitals states which are energetically well-separated form other states [56–58]. The estimated parameters are $U = 2.474$ eV and $J_{\rm H} = 0.106$ eV which were further used in our multi-band Hubbard model.

III. Results

A. Structural analysis and electronic properties

Under a large $\Delta_i^{\rm CF}$, the low energy space Rh-4d^5 ions can be described by a single hole within the t_{2g} manifold with effective spin moment $s = 1/2$ and effective orbital angular moment $L' = 1$. The spin-orbit coupling then leads to an effective total angular momentum of $\boldsymbol{J_{\rm eff}}$ = $\boldsymbol{s}$ - $\boldsymbol{L'}$ resulting in doubly degenerate pseudospin-1/2 states forming low-energy space in this material. This is schematically shown in Fig. 1(a). However, the lowering of cubic O_h symmetry of octahedron due additional $\Delta^{\rm CF}_{\rm tri.}$($\Delta^{\rm CF}_{\rm tet.}$) terms can invalidate this picture. Hence it is important to first examine whether Rh-O_6 octahedra in Sr_4RhO_6 retains the O_h symmetry as was proposed earlier in Ref [46].

In this experimental crystal structure, all the six Rh-O bond lengths are $\sim$ 2.044 Å while O-Rh-O bond angles are quite close to the ideal 90° with the largest deviation being 0.1°. However, full structural optimization with the magnetic ground state in our DFT calculation brings substantial changes in a and b lattice constants along with the changes in the local octahedral environment. The optimization enhanced a and b lattice constants to 10.046 Å and also all the six Rh-O bond lengths elongated to 2.109 Å. The structural optimization also alters the O-Rh-O bond angles to 92.28 and 87.72°(see Fig. 1(b)). Also, out of eight Sr neighbors in the extended environment of Rh atoms, two "apical" Sr atoms along c axis are at 2.952 Å distance while other "non-apical" six are at 3.340 Å in the optimized structure. This is shown in Fig. 1(b) (short Rh-Sr distances are along A-bonds and long ones are along B/C/D-bonds). These two kinds of Rh-Sr distances were 2.960 and 3.238 Å in the starting structure. Almost similar Rh-Rh 1NN distances $\sim$ 5.98/6.0 Å of all the 8 bonds before optimization has changed substantially now to $\sim$ 5.9 and 6.13 Å for two A-bonds, and six B/C/D bonds respectively. Thus optimization of structure results in substantial changes in Rh-O, non-apical Rh-Sr, and overall Rh-Rh bond lengths and is consistent with enhancement of a and b lattice constants.

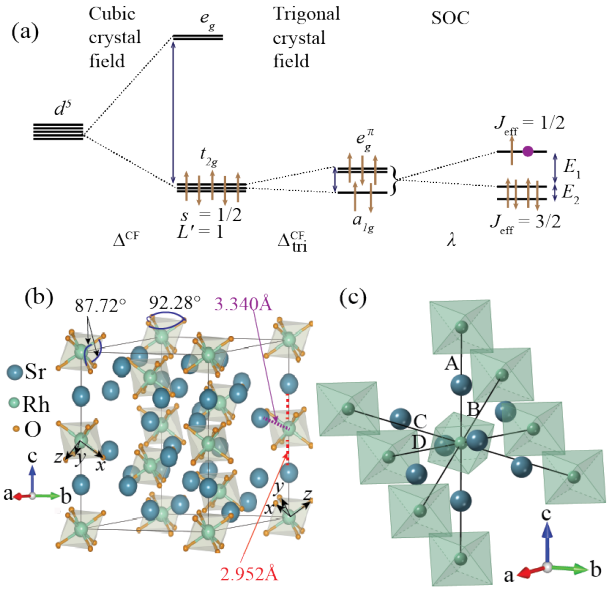


FIG. 1. (a) $J_{\rm eff}$ picture for a d^5 system arising from octahedral crystal field ($\Delta^{\rm CF}$) and spin-orbit coupling (λ). Additional splitting of t_{2g} states into a singlet a_{1g} and a doublet e_g^π due to trigonal like distortions ($\Delta^{\rm CF}_{\rm tri.}$). SOC further leads to a $J_{\rm eff}$ =1/2 doublet and two $J_{\rm eff}$ =3/2 doublets separated by E_2. E_1 is the energy separation between $J_{\rm eff}$ =1/2 and closest $J_{\rm eff}$ =3/2 doublet. (b) Side view of Sr_4RhO_6 crystal structure. Spatially separated octahedron are evident. Local x, y, and z axes on two of the octahedron are shown. a, b and c are the global crystallographic axes. Two kinds of color-coded Rh-Sr bonds along with O-Rh-O bond angles obtained after optimization of the crystal structure are shown. (c) Extended local environment (including Sr atoms) around an Rh atom in Sr_4RhO_6. Four types of Rh-Rh nearest neighbors A, B, C, and D-bonds with Rh-O Octahedra on these bonds are also shown.

In order to understand how these changes in crystal structure affect the CF, we set up a TB model with d orbital basis of $\psi^\dagger = [d^\dagger_{z^2}, d^\dagger_{x^2-y^2}, d^\dagger_{xz}, d^\dagger_{yz}, d^\dagger_{xy}]$ using Wannierization procedure as mentioned in Methods section (fitting is shown in Fig. 2(a)). CF matrix $\Delta_i^{\rm CF}$ obtained from $H_{\rm TB}$ is given in Eq. 1. Entries in the matrix are in the unit of eV. One can clear see that this CF matrix obeys C_3 symmetry restriction as the off-diagonal elements within the t_{2g} (colored entries in the matrix) manifold have nearly the same absolute values within an error bar of 5 meV.

$$\Delta_i^{\rm CF} = \begin{bmatrix} 2.5379 & -0.0006 & -0.1292 & 0.0987 & -0.0517 \\ -0.0006 & 2.5474 & 0.0150 & -0.0088 & -0.0762 \\ -0.1292 & 0.0150 & 0.1127 & 0.0499 & 0.0531 \\ 0.0987 & -0.0088 & 0.0499 & 0.1055 & -0.0547 \\ -0.0517 & -0.0762 & 0.0531 & -0.0547 & 0.1138 \end{bmatrix} \quad (1)$$

By diagonalizing this matrix one can find that the t_{2g}-e_g crystal field splitting ($\Delta_i^{t_{2g}-e_g}$) is $\sim$ 2.630 eV while the triply degenerate t_{2g} splits into a a_{1g} singlet and e_g^π doublet by $\Delta_{\rm tri}^{\rm CF} \sim 160$ meV with doublet being higher in energy than the singlet. The corresponding eigenvectors are graphically represented in Fig. 2(b), where each column in the 5 × 5 graph represents an eigenvector with row representing absolute weight of individual orbitals. This representation clearly highlights the nature of $\Delta_i^{\rm CF}$ in Sr_4RhO_6 which has been depicted in Fig. 1(a).

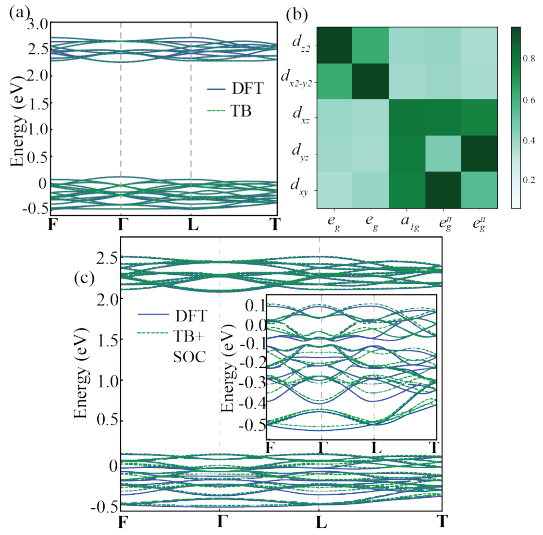


FIG. 2. (a) Band structure plot from the *ab initio* and Wannier-based TB model calculations considering all the Rh *d* orbitals in the basis. (b) Graphical representation of eigenvectors of matrix in Eq. 1. In column-wise representation of eigenvectors each row represents absolute weight of individual orbitals. Labeling of eigenstates is done in accordance of Fig. 1(a). (c) Fitting of *ab initio* SOC band structure with Wannier based tight binding model after including onsite SOC term in the Hamiltonian. The inset shows the fitting near the Fermi level which is set to zero in all the plots.

This particular form of $\Delta_i^{\rm CF}$ can be understood as follows. The shorter "apical" Sr-Rh bond passes through the center of two triangular faces of Rh-O_6 octahedra as shown in Fig. 1(b)-(c). This bond is also one of the four three-fold rotational symmetry (C_3) axis of the Rh-O_6 octahedra. The electrostatic repulsion along these shorter bonds behaves as compressing strain causing changes in Rh-O bond lengths and O-Rh-O bond angles. This is analogous to the case of trigonal distortions where bond distortions take place along one of the four C_3 axes of the octahedra. Thus, in Sr_4RhO_6, an extended anisotropic environment of Sr atoms produces a non-spherical crystalline potential responsible for additional $\Delta_{\rm tri.}^{\rm CF}$ of Rh-O_6 octahedra. The cubic O_h symmetry, then lowers to C_{3i} (-3) in this case.

Distortions like $\Delta_{\rm tri.}^{\rm CF}$ tend to lower the energy separation between $J_{\rm eff}$ =1/2 and 3/2 states. This brings a genuine concern about effect of SOC on electronic structure of Sr_4RhO_6 and whether the strength of SOC in Sr_4RhO_6 is sufficient enough to separate out these two states. To examine this point, we calculated the *ab initio* band structures for three cases, (i) non-magnetic, (ii) with SOC, and (iii) with SOC + U. SOC was included at the self-consistent level in these calculations.

In Fig. 3, we only show the bands near the Fermi level which are dominantly contributed by t_{2g} orbitals. We projected the band structures onto $J_{\rm eff}$ states with the form given below.

$$\left|\frac{1}{2},\pm\frac{1}{2}\right\rangle = \frac{1}{\sqrt{3}}\left(\mp|d_{xy},\pm\tfrac{1}{2}\rangle \mp i|d_{xz},\mp\tfrac{1}{2}\rangle - |d_{yz},\mp\tfrac{1}{2}\rangle\right)$$
$$\left|\frac{3}{2},\pm\frac{3}{2}\right\rangle = \frac{1}{\sqrt{2}}\left(-i|d_{xz},\pm\tfrac{1}{2}\rangle \mp |d_{yz},\pm\tfrac{1}{2}\rangle\right)$$
$$\left|\frac{3}{2},\pm\frac{1}{2}\right\rangle = \frac{1}{\sqrt{6}}\left(2|d_{xy},\pm\tfrac{1}{2}\rangle - i|d_{xz},\mp\tfrac{1}{2}\rangle \mp |d_{yz},\mp\tfrac{1}{2}\rangle\right)$$

There are mainly two points to be noticed in Fig. 3. First that inclusion of SOC substantial changes the band structure. This is apparent from comparing non-spin polarised band structure plot in Fig. 3(a) and SOC included band structure plot shown in Fig. 3(b). In particular, SOC leads to separation of $J_{\rm eff} = 1/2$ bands near -0.1 eV (red box in Fig. 3(b)) from the other bands ($J_{\rm eff} = 3/2$ bands) near -0.1 eV. Inclusion of U on Rh d states further contributes to this band separation as shown in Fig. 3(c) and the dominant contribution near the Fermi level now clearly shown to have $J_{\rm eff} = 1/2$ character. Imposition of the magnetic ground state in band structure calculation (not shown) fully opens the gap at the Fermi level making it insulating. This is similar to the case of α-$RuCl_3$ [35]. From this analysis of electronic structure, one can conclude that the electronic structure of Sr_4RhO_6 is the combined efforts of U, SOC, and magnetism. Having examined the role of SOC, one can further quantify the $J_{\rm eff}$ =1/2 and 3/2 states admixture due to $\Delta_{\rm tri.}^{\rm CF}$ by considering a multi-band Hubbard model for an isolated Rh^{+4} ion. This is discussed in the next section.

B. Onsite Hamiltonian and the atomic features

One way to estimate the extent of mixing between the $J_{\rm eff}$ =1/2 and 3/2 states is by calculating the projection of a "pure" $J_{\rm eff}$ =1/2 and 3/2 states for the case when $\Delta_{\rm tri.}^{\rm CF} = 0$ onto the "true" $J_{\rm eff}$ =1/2 obtained with Eq. 1. These states are atomic features and hence can be described in an isolated atom limit. In this limit, a multi-band Hubbard Hamiltonian at site, i in the five-orbital

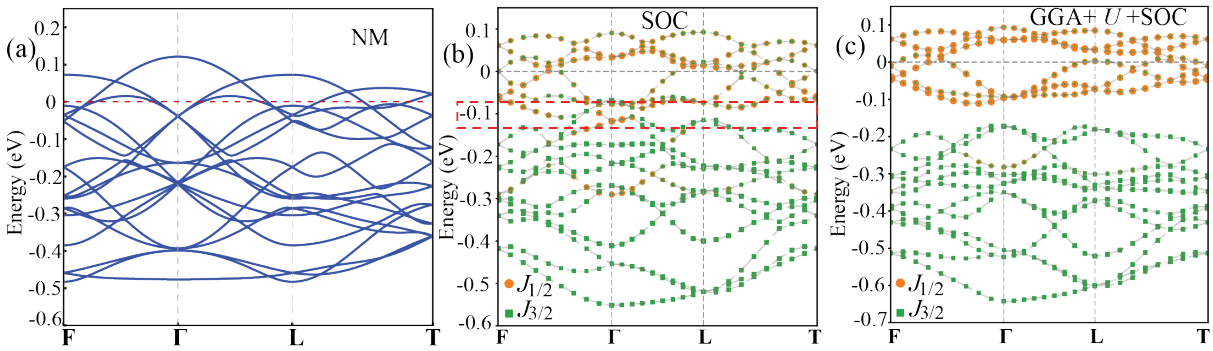


FIG. 3. *Ab initio* band structure plots near the Fermi level. Case of (a) non-magnetic (NM), (b) SOC included and (c) SOC + U (on Rh d orbitals) band structure projected onto $J_{\rm eff}$ states. Fermi level is set to 0 eV. The fined dashed box in (b) shows the energy window of where separation of $J_{\rm eff}$ =1/2 bands from other $J_{\rm eff}$ =3/2 bands take place with inclusion of SOC. Clear $J_{\rm eff}$ = 1/2 character is apparent at the Fermi level in (c).

basis reads as,

$$\begin{aligned} H_0 &= H_{\rm cf} + H_{\rm soc} + H_{\rm int} \\ &= \sum_{i,\sigma} \psi^\dagger_{i\sigma} \Delta_i^{\rm CF} \psi_{i\sigma} + \sum_i \lambda \boldsymbol{L}_i \cdot \boldsymbol{s}_i \\ &+ \frac{U}{2} \sum_{i,\alpha} n_{i\alpha\sigma} n_{i\alpha\sigma'} + \frac{U'}{2} \sum_{i,\alpha\neq\beta} n_{i\alpha} n_{i\beta} \\ &- \frac{J_{\rm H}}{2} \sum_{i,\sigma,\sigma',\alpha\neq\beta} \psi^\dagger_{i\alpha\sigma} \psi_{i\alpha\sigma'} \psi^\dagger_{i\beta\sigma'} \psi_{i\beta\sigma} \\ &- \frac{J'}{2} \sum_{i,\sigma\neq\sigma',\alpha\neq\beta} \psi^\dagger_{i\alpha\sigma} \psi_{i\beta\sigma'} \psi^\dagger_{i\alpha\sigma'} \psi_{i\beta\sigma} \end{aligned} \quad (2)$$

In above expression, U/U' are intraorbital/interorbital Hartree energies; and $J_{\rm H}$ and J' are Hund's coupling and pair hopping interaction, respectively. Rotational invariance in the isolated atom limit dictates the relationships: $U' = U$ - $2J_{\rm H}$ and $J_{\rm H} = J'$. We use U = 2.474 eV and $J_{\rm H}$ = 0.106 eV which are estimated from cRPA as mentioned in the Methods section and λ = 140 meV is considered. We diagonalize the above Hamiltonian considering five electrons of Rh^{+4} ions which give a total of 252 eigenstates, the lowest two and the next four of which are the $J_{\rm eff}$ =1/2 states and $J_{\rm eff}$ =3/2 states, respectively.

	$\langle\phi'_\alpha\|\phi_\beta\rangle$	
$\langle\phi'_\alpha\|$	$\|\phi_1\rangle$	$\|\phi_2\rangle$
1	0.901	0.352
2	0.352	0.901
3	0.162	0.056
4	0.056	0.162
5	0.101	0.117
6	0.117	0.101

TABLE I. Projections of $J_{\rm eff}$ =1/2, 3/2 states obtained when $\Delta^{\rm CF}_{\rm tri.}$ = 0, onto $J_{\rm eff}$ =1/2 states with *true* CF from Eq. 1. These states are obtained from exact-diagonalization of the Hamiltonian in Eq. 2.

For $\Delta^{\rm CF}_{\rm tri.}$ = 0, t_{2g}-e_g splitting was fixed at 2.790 eV and all the off-diagonal matrix elements were zeroed in Eq. 1. The lowest six states in this case are represented by $\{\phi'_\alpha\}$, α = 1, 6 while lowest two states obtained using *true* CF from Eq. 1 are labelled as $\{\phi_\beta\}$, β = 1-2. The projections $\langle\phi'_\alpha|\phi_\beta\rangle$ are listed in Table I. From the table, since $|\langle\phi'_\alpha|\phi_\beta\rangle|^2 = 0.811$ for $\delta_{\alpha\beta}$ = 1, 2, one can conclude that the $J_{\rm eff}$ =1/2 states retain their major weight despite a substantial $\Delta^{\rm CF}_{\rm tri.}$, validating applicability of $J_{\rm eff}$ = 1/2 picture in Sr_4RhO_6. The non-zero value of projections $|\langle\phi'_\alpha|\phi_\beta\rangle|^2$ ($\sim$ 0.026/0.010) for α = 3-6, β = 1-2 indicates a small admixture of $J_{\rm eff}$ =1/2 and 3/2 states due to $\Delta^{\rm CF}_{\rm tri.}$. We find small changes of $\sim$ 4 % in these projections for λ = 90 meV.

One of the quantities which can be measured from the resonant inelastic X-ray scattering experiments are the single-point excitations represented by sharp peaks in the scattering intensity in the relevant energy range. It can be a direct probe for cubic symmetry lowering of the Rh-O_6 octahedra in Sr_4RhO_6. Theoretically, such a low-lying crystal field-assisted many-body excitations bear a close resemblance to the eigenvalues obtained from diagonalization of many-body Hamiltonian in Eq. 2. For Sr_4RhO_6, analysis of eigenvalue reveals that the $J_{\rm eff}$ = 3/2 states split into two doublets by E_2 = 0.133 eV (see Fig. 1(a)) which would otherwise be four-fold degenerate if $\Delta^{\rm CF}_{\rm tri.}$ = 0. Energy separation of the $J_{\rm eff}$ = 1/2 doublet with the lower $J_{\rm eff}$ = 3/2 doublet is E_1 = 0.181 eV. It can also be observed that E_1 is $\sim$ 30 meV smaller than the expected value of $\frac{3}{2}\lambda$ due to finite $\Delta^{\rm CF}_{\rm tri.}$. From the higher $J_{\rm eff}$ = 3/2 doublets, the next single ion excitation is at $\sim$ 1.695 eV. From this point, a broad continuum of states with energy separations of few meV in the window of $\sim$ 165 meV are found in our calculations. Having investigated the electronic properties of Sr_4RhO_6, we now discuss its magnetic properties in the next section.

C. Magnetism

We start by projecting the Hamiltonian in Eq. 2 to the pseudo-spins $J_{1/2}$ subspace and introduce hoping ($H_{\rm hop}$)

as perturbation. The hopping amplitudes are extracted from $H_{\rm TB}$ and are listed in Appendix V. In the limit $U \gg t$, the second-order perturbation term brings,

$$H^{(2)} = \sum_{ij} \sum_{\alpha\beta\alpha'\beta'} \mathcal{H}(i,j)_{\alpha\beta\alpha'\beta'} |i\alpha, j\beta\rangle \langle i\alpha', j\beta'|,$$
$$\mathcal{H}(i,j)_{\alpha\beta\alpha'\beta'} = \sum_{kl} \sum_{\gamma\lambda} \frac{1}{\Delta E} \langle i\alpha, j\beta|H_{\rm hop}|k\gamma, l\lambda\rangle \langle k\gamma, l\lambda|H_{\rm hop}|i\alpha', j\beta'\rangle, \quad (3)$$

where $1/\Delta E = \frac{1}{2}[1/(E_{i\alpha} + E_{j\beta} - E_{k\lambda} - E_{l\gamma})$. Here, $|i\alpha, j\beta\rangle$ and $|i\alpha', j\beta'\rangle$ are two-site states made of $J_{1/2}$ doublets, and $|k\lambda, l\gamma\rangle$ are two-site excited states with d^6 and d^4 configurations with Hilbert space dimensions of 210 for both. $H_{\rm hop}$ connects a two-site ground state to these excited states. The eigenstates of isolated Rh ions with 4 and 6 -d electrons are obtained again by exact diagonalization.

One can represnt the pseudo-spins $J_{1/2}$ as $S^\mu = \langle i\alpha|\boldsymbol{J}^{\boldsymbol{\mu}}_{\boldsymbol{i,\ \rm eff}}|i\beta\rangle$ which are the expectation values of pseudospin $J^\mu_{\rm eff}$ operators with $\mu = 0, x, y, z$. Here, $\boldsymbol{J}^{\boldsymbol{0}}_{\boldsymbol{\rm eff}} = \mathbb{1}_{2\times2}$ is the matrix representation of operator $\boldsymbol{J}^{\boldsymbol{0}}_{\boldsymbol{\rm eff}}$. Using it, Eq. (3) can be mapped to a spin Hamiltonian of the form,

$$H_{\rm spin} = S^\mu_i \Gamma(i,j)^{\mu\nu} S^\nu_j$$
$$= \Gamma(i,j)^{\mu\nu} \phi^\dagger_{i\alpha} S^\mu_{\alpha\alpha'} \phi_{i\alpha'} \phi_{j\beta} S^\nu_{\beta\beta'} \phi^\dagger_{j\beta},$$

In the above expression, summation over all repeated indexes is implied. The map can be achieved by solving the linear equations,

$$- S^\mu_{\alpha\alpha'} S^\nu_{\beta\beta'} \Gamma(i,j)^{\mu\nu} = \mathcal{H}(i,j)_{\alpha\beta\alpha'\beta'}$$

Here, degeneracy of the Kramers doublet leads $\Gamma^{0\mu} = \Gamma^{\mu 0} = 0$. Thus, the most general form of exchange interaction matrix on an Rh-Rh bond $l \in (i,j)$ is defined as,

$$\Gamma_l = \begin{pmatrix} J+\zeta & \eta+D & \eta'-D' \\ \eta-D & J-\zeta & \eta''+D'' \\ \eta'+D' & \eta''-D'' & J+K \end{pmatrix} \quad (4)$$

In the above expression, J, K, and η/η' are the Heisenberg, Kitaev and off-diagonal interaction terms between the pseudospins-1/2, while ζ is the diagonal anisotropic term. DMI is represented by (D, D', D'') vector.

The Rh atoms forms a body-centered cubic lattice in Sr_4RhO_6 and thus each Rh atom has eight 1NNs. Based on the nature of magnetic interactions between different 1NNs, we subdivide the Rh-Rh bonds into three distinct categories which are indicated as A/B/C/D bonds in Fig. 1(c). Values of magnetic interactions are listed in Table II. For bond A and C, the Γ_l matrix acquire a more symmetric form since on these bonds $\zeta = \eta = \eta' = \eta'' = D = D' = D'' = 0$. However, the magnetic interactions on these two bonds differ in their strengths. On B-bond, $\Gamma_{\rm B}$ takes the general form of Eq. 4 and $\Gamma_{\rm D}$ can be obtained by simply taking the transpose of $\Gamma_{\rm B}$.

Several remarks are in order. First, one can see that the strength, as well as signs of interactions, differ for different bonds. For example, for A and C bonds J, η, and η' are antiferromagnetic while for B-bond they are ferromagnetic and the antiferro Kitaev coupling is stronger on B-bond than the others. We emphasize that the antiferromagnetic Kitaev coupling in Sr_4RhO_6, although smaller, distinctly differs from the previous reports on iridates and α-$RuCl_3$ [36, 54]. Second, quite interestingly, DMI appears on B and D bonds in the centrosymmetric structure of Sr_4RhO_6. However, D, D', and D'' have opposite signs on these two bonds. We attribute appearance of DMI to the local inversion symmetry breaking due to anisotropic crystalline potential produced by Sr atoms in the extended environment around Rh atoms shown in Fig. 1(c). The hopping pathways for the first nearest symmetry in-equivalent Rh-Rh neighbors gets influenced by the crystalline potential produced by this extended environment resulting in $T^t_{ij} \neq T_{ij}$ form of hopping matrix in appendix V. Disappearance of DMI on A and C bond is merely an artifact of local coordinate system that we choose for our $H_{\rm TB}$. For DMI between two sites, it is always possible to make a local rotation of the spin coordinate axes at one of the sites to "gauge" away this interaction by rotating the coordinates around the axis of the DM-vector by an angle corresponding to the classical canting angle [59]. We verify this point by choosing a set of different local axes in which DMI appears at both A and C bonds albeit smaller than B and D bonds. Third, one may think that the Sr^{+2} ions on A-bond may mediate superexchange interaction between Rh atoms through their s orbitals. However, on the contrary, we find highly suppressed interactions on this bond suggesting a destructive role of the anisotropic crystalline potential of the Sr^{+2} on magnetic interactions. Fourth, we found large off-diagonal terms on some of the Rh-Rh bonds. This is similar to the case of iridates and α-$RuCl_3$ [54] resulting from substantial $\Delta^{\rm CF}_{\rm tri.}$ distortions present in all these materials. Based on the two particularly noticeable features in the first two points, *viz-a-viz* antiferromagnetic Kitaev terms and appearance of DMI,

	$\lambda = 90$ meV			$\lambda = 140$ meV			$\lambda = 174$ meV		
Term	A	B	C	A	B	C	A	B	C
J	0.149	−0.519	4.262	0.301	−0.109	3.250	0.402	−0.021	2.975
K	0.010	−1.737	0.473	0.015	−1.596	0.257	0.017	−1.544	0.193
ζ	−0.016	−0.488	−0.199	−0.017	−0.538	−0.125	−0.017	−0.555	−0.101
η	0.022	−2.246	1.066	0.017	−1.829	0.460	0.011	−1.686	0.296
η'	−0.016	1.040	−0.873	−0.014	0.683	−0.348	0.000	0.564	−0.207
η''	0.025	−1.231	0.723	0.019	−0.899	0.271	0.012	−0.784	0.154
D	0.000	−1.377	0.000	0.000	−0.666	0.000	0.000	−0.472	0.000
D'	0.000	2.518	0.000	0.000	1.608	0.000	0.000	1.332	0.000
D''	0.000	−2.303	0.000	0.000	−1.325	0.000	0.000	−1.041	0.000

TABLE II. Estimated first neighbor (NN) Heisenberg J, Kitaev K and diagonal ζ and off-diagonal η, η', η'' anisotropic terms for Sr_4RhO_6 given in meV. The second nearest neighbor interactions were found to be negligibly small (< 0.01 meV). Parameters used are $U = 2.474$ eV, $J_H = 0.106$ eV and three values of $\lambda = 90$, 140, 174 meV.

one may consider Sr_4RhO_6 a distinct $4d$ magnetic material.

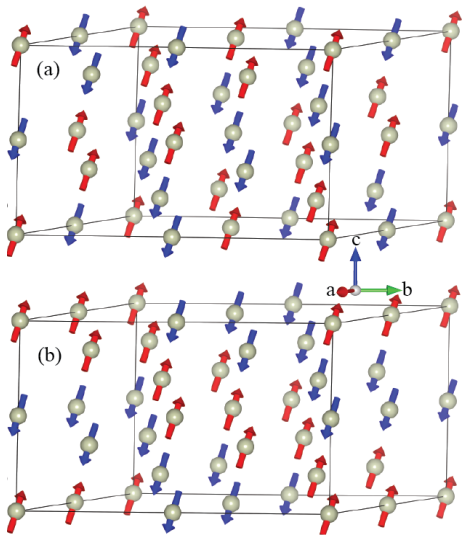


FIG. 4. (a) Experimentally proposed magnetic ground state of Sr_4RhO_6. (b) Classical ground state obtained from optimization of classical ground state using exchange interactions of Table II. Color coded spin orientation of only Rh lattice is shown here.

Varying the magnitude of SOC strength λ in our model does not change the interactions at a qualitative level. Estimated magnetic interactions for $\lambda = 90$, 195 meV are listed in Table II along with values for $\lambda = 140$ meV. The trend here is that with increase of λ, absolute values of all the magnetic interactions decreases except the AFM J term on A bond.

Magnetic interaction of Table II are used to optimize the classical magnetic state using SpinW package [60]. The obtained magnetic ground state, represented by ordering vector ∼(1.0 0.5 0), is shown in Fig. 4(b) along with the experimentally proposed one in Fig. 4(a). The antiferromagnetic state obtained in our calculations successfully captures most of the experimental features. In the experimental magnetic structure, the spin arrangement on Rh-Rh bonds(Fig. 1(c)), A and B are antiferromagnetic while on C and D it is ferromagnetic. Optimized magnetic state in Fig. 4(b) from our calculations retains antiferromagnetic coupling on A and ferromagnetic coupling at D bonds. However, this configuration differs from the one shown in Fig. 4(a) on bonds B and C where the spin arrangement in the two cases are just opposite to each other i.e. on B-bond the coupling is ferro while on C-bond it is antiferromagnetic in our optimized structure. Swapping the interactions at bonds B and C does not bring the experimentally observed ground state indicating a joint meticulous effort of all the magnetic interactions to bring the ground state. We find a slight deviation of magnetic moments from the ac plane mainly due to the presence of off-diagonal terms like $\eta/\eta'/\eta''$ and DMI. This is consistent with the experimental finding of small tilting from c axis [46]. Our optimized magnetic configuration is energetically close to the experimentally proposed one with the former stabilized by 1.552 meV/spin. The second and third neighbor magnetic interactions are found to be negligibly small in Sr_4RhO_6 and do not bring any distinguishable change in the optimization of the magnetic ground state. Thus we ignore them in further calculations of spin-wave spectra.

Here, we would like to comment that the scale of magnetic ordering temperature of a material depends on various parameters like the strength of exchange interactions, number of neighbors, their corresponding exchange contributions, and spatial dimensions of the magnetic lattice. Although, the magnetic lattice of Rh atoms in Sr_4RhO_6 form a three-dimensional bulk structure with eight first magnetic neighbors, the strongly frustrated anisotropic nature of bond-dependent magnetic interactions might be the reason behind its experimentally observed low T_N of ∼ 7.5 K. We used the classical Monte Carlo technique implemented in SpinW package [60] to estimate T_N for Sr_4RhO_6. Estimated value $T_N = 10.5$ K for interactions corresponding to $\lambda = 140$ meV in Table II is in close agreement with the experimental observation.

D. Spin-wave spectra

We further use the magnetic interactions listed in Table II in linear spin-wave theory to obtain the spin-wave spectra using SpinW package [60]. Obtained spectra along various reciprocal space directions is shown in Fig. 5.

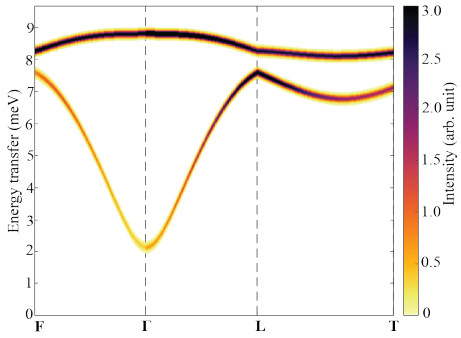


FIG. 5. Spin wave spectra of Sr_4RhO_6 obtained within linear spin wave theory considering magnetic interactions of Table II.

Several points are to be noted about the spectra. First, one can see that the spectra have gaped along all directions in reciprocal space with a Goldstone gap of $\sim$ 2 meV. This feature of spin-wave spectra may be caused by the breakdown of $SU(2)$ symmetry of the isotropic Heisenberg Hamiltonian. Such a symmetry breaking can be a result of additional Ising like Kitaev terms and/or diagonal/off-diagonal anisotropic terms like ζ, η, η' and η''. Second, one branch $\sim$ 8 meV in the spectra appears to be dispersion-less. It is separated from the dispersing branch by $\sim$ 0.5 meV. Such a feature has previously been observed from the inelastic neutron scattering experiments on some of the cobaltates [16], pertinent material candidates for Kitaev physics [23]. Third, it can observe that the spin-wave spectra near $\mathbf{\Gamma}$ point is quadratic in nature. This is in contradiction to the expected linear dispersion of spin-wave dispersion for an antiferromagnetic ground state.

In order to investigate the origin of previously mentioned features of spin-wave spectra of Sr_4RhO_6, we break it down to the contribution of either individual or a specific combination of magnetic interactions and the plots are shown in Fig. 6. Such an analysis can provide useful insights as has been shown in Ntallis *et. al.* [61] for the case of $NaOsO_3$.

Considering J and K terms together, we immediately obtain both branches with a lower branch, at $\mathbf{\Gamma}$, showing the linear dispersion behavior of an antiferromagnet. The plot is shown in Fig. 6(a). However, the spectra are barely gaped in this case due to dominant J over K and which is also responsible for the dispersion width of $\sim$ 5.5 meV of the lower branch. Consideration of K-only term in the Hamiltonian produces a completely flat branch at $\sim$ 4 meV (not shown) consistent with the previous theoretical study on Kitev model [62]. ζ-only term indeed causes the gap opening along with deviation towards a quadratic dispersion at $\mathbf{\Gamma}$ of the lower branch and as shown in Fig. 6(b). However, the energy scale, in this case, is smaller than that of the original spectra in Fig. 5. A combination of $J+K+\zeta$ (Fig. 6(c)) reproduces some of the features in the more or less similar spectral windows as that of the original spectra. However, the dispersion width and nature of the lower branch, in this case, are inconsistent with the original one in Fig 5. Additionally, near $\mathbf{\Gamma}$, dispersion of the lower branch appears to be further deviating from quadratic to higher powers of $\boldsymbol{k}$. The terms $D + D' + D'' + \eta + \eta' + \eta''$ produces similar but relatively flatter branches than the ζ terms and is shown Fig. 6(d). The spectral energy window, in this case, is similar to that of $J + K + \zeta$ term. Thus one can say conclusively that the dominant off-diagonal terms are mainly responsible for the gap in spin-wave spectra of Sr_4RhO_6 while the diagonal anisotropic term decides the nature of dispersion near $\mathbf{\Gamma}$ point in spin-wave spectra of Sr_4RhO_6. The overall spectra which resemble a typical magnetic system with strong frustration is a joint effort of all the terms of magnetic Hamiltonian.

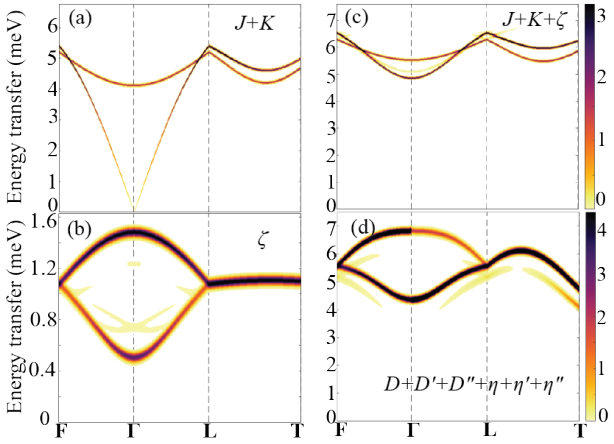


FIG. 6. Breakdown of spin-wave spectra shown in Fig. 3 to individual contributions of combination of various magnetic interactions. Spectra from, (a) $J+K$ terms, (b) only diagonal anisotropic term ζ, (c) $J + K + \zeta$ terms and (d) $D + D' + D$" $+ \eta + \eta' + \eta''$ terms from Table II.

IV. Conclusion

In the quest for new Kitaev candidates, in this work, we have investigated the electronic and magnetic properties of Sr_4RhO_6. Through *ab initio* calculations and a TB model, we show the lowering of cubic symmetry of RhO_6 octahedra due to additional trigonal-like distortions which are in contradiction to the previous experimental proposal. Using the exact diagonalization technique, we show that despite such a distortion, electronic and magnetic properties of Sr_4RhO_6 can be well described

with the pseudo-spin 1/2 framework. The magnetic interactions between these pseudo-spins were found to be highly bond-dependent anisotropic in nature. We found two particularly noticeable features of the 1NN magnetic interactions in Sr_4RhO_6 which are, appearance of antiferromagnetic Kitaev term and DMI. This may place Sr_4RhO_6 in a distinct class of materials as previously proposed Kitaev candidates shown to have ferromagnetic Kitaev couplings and DMI appears on the 2nd neighbor bonds [54]. The analysis of spin-wave spectra obtained using linear spin-wave theory considering these interactions reveals the crucial role of diagonal and off-diagonal magnetic interactions in producing a gaped spectrum of Sr_4RhO_6. Our theoretical study provides deeper insights about the coupling among structural, electronic and magnetic degrees of freedom in these compounds and calls for further experimental investigations.

V. Acknowledgment

We have greatly benefited from stimulating discussions with Dr. Stephen M Winter and gratefully acknowledge his critical reading of our manuscript and valuable feedback. We acknowledge the financial support from the National Key R & D Program of China (Grant No.2018YFA0305601), National Natural Science Foundation of China (Grant No. 11725415), and Innovation Program for Quantum Science and Technology (Project No. 2021ZD0302600). This work is also supported partially by the China Postdoctoral Science Foundation (No.2022M710231) awarded to Q. Gu.

Appendix A: First neighbors Rh-Rh hopping amplitudes in Sr_4RhO_6 expressed in the basis ($d^\dagger_{z^2}$, $d^\dagger_{x^2-y^2}$, $d^\dagger_{xz}$, $d^\dagger_{yz}$, $d^\dagger_{xy}$).

A-bond

$$\begin{pmatrix} -0.0251 & -0.0042 & -0.0015 & 0.0144 & 0.0217 \\ -0.0042 & 0.0270 & 0.0182 & 0.0131 & -0.0094 \\ -0.0015 & 0.0182 & -0.0288 & 0.0240 & -0.0319 \\ 0.0144 & 0.0131 & 0.0240 & -0.0369 & 0.0263 \\ 0.0217 & -0.0094 & -0.0319 & 0.0263 & -0.0199 \end{pmatrix}$$

B-bond

$$\begin{pmatrix} 0.0245 & 0.0006 & -0.0302 & 0.0517 & 0.0141 \\ 0.0368 & -0.0040 & -0.0626 & 0.0285 & 0.0339 \\ -0.0334 & -0.0077 & -0.0100 & 0.0009 & -0.0192 \\ -0.0791 & -0.0004 & 0.0633 & 0.0175 & 0.0087 \\ 0.0476 & -0.0294 & 0.0256 & 0.0130 & 0.0033 \end{pmatrix}$$

C-bond

$$\begin{pmatrix} -0.0083 & 0.0134 & -0.0001 & -0.0217 & -0.0419 \\ 0.0134 & -0.0245 & 0.0618 & 0.0233 & 0.0622 \\ -0.0001 & 0.0618 & -0.0173 & -0.0057 & 0.0128 \\ -0.0217 & 0.0233 & -0.0057 & -0.0194 & 0.0103 \\ -0.0419 & 0.0622 & 0.0128 & 0.0103 & -0.0684 \end{pmatrix}$$

TABLE A-1. First neighbor Rh-Rh hopping amplitudes on different types of bonds shown in Fig. 1(c)

.

[1] M. Z. Hasan and C. L. Kane, Colloquium: Topological insulators, Rev. Mod. Phys. **82**, 3045 (2010).

[2] M. Z. Hasan and J. E. Moore, Three-dimensional topological insulators, Annual Review of Condensed Matter Physics **2**, 55 (2011).

[3] X.-L. Qi and S.-C. Zhang, Topological insulators and superconductors, Rev. Mod. Phys. **83**, 1057 (2011).

[4] W. Witczak-Krempa, G. Chen, Y. B. Kim, and L. Balents, Correlated quantum phenomena in the strong spin-orbit regime, Annual Review of Condensed Matter Physics **5**, 57 (2014).

[5] J. G. Rau, E. K.-H. Lee, and H.-Y. Kee, Spin-orbit physics giving rise to novel phases in correlated systems: Iridates and related materials, Annual Review of Condensed Matter Physics **7**, 195 (2016).

[6] P. Anderson, Resonating valence bonds: A new kind of insulator?, Mater. Res. Bull **8**, 153 (1973).

[7] J. Kim, D. Casa, M. H. Upton, T. Gog, Y.-J. Kim, J. F. Mitchell, M. van Veenendaal, M. Daghofer, J. van den Brink, G. Khaliullin, and B. J. Kim, Magnetic excitation spectra of sr_2iro_4 probed by resonant inelastic x-ray scattering: Establishing links to cuprate superconductors, Phys. Rev. Lett. **108**, 177003 (2012).

[8] G. Khaliullin, W. Koshibae, and S. Maekawa, Low energy electronic states and triplet pairing in layered cobaltate, Phys. Rev. Lett. **93**, 176401 (2004).

[9] H. Y. Hwang, Y. Iwasa, M. Kawasaki, B. Keimer, N. Nagaosa, and Y. Tokura, Emergent phenomena at oxide interfaces, Nature Materials **11**, 103 (2012).

[10] G. Jackeli and G. Khaliullin, Mott Insulators in the Strong Spin-Orbit Coupling Limit: From Heisenberg to a Quantum Compass and Kitaev Models, Phys. Rev. Lett. **102**, 017205 (2009).

[11] A. Kitaev, Anyons in an exactly solved model and beyond, Ann. Phys. **321**, 2 (2006), january Special Issue.

[12] L. Clark and A. H. Abdeldaim, Quantum spin liquids from a materials perspective, Annual Review of Materials Research **51**, 495 (2021), https://doi.org/10.1146/annurev-matsci-080819-011453.

[13] H. Takagi, T. Takayama, G. Jackeli, G. Khaliullin, and S. E. Nagler, Concept and realization of kitaev quantum spin liquids, Nature Reviews Physics **1**, 264 (2019).

[14] H. Liu and G. Khaliullin, Pseudospin exchange interactions in d^7 cobalt compounds: Possible realization of the Kitaev model, Phys. Rev. B **97**, 014407 (2018).

[15] R. Sano, Y. Kato, and Y. Motome, Kitaev-Heisenberg Hamiltonian for high-spin d^7 Mott insulators, Phys. Rev. B **97**, 014408 (2018).

[16] M. Songvilay, J. Robert, S. Petit, J. A. Rodriguez-Rivera, W. D. Ratcliff, F. Damay, V. Balédent, M. Jiménez-Ruiz,

P. Lejay, E. Pachoud, A. Hadj-Azzem, V. Simonet, and C. Stock, Kitaev interactions in the Co honeycomb antiferromagnets $Na_3Co_2SbO_6$ and $Na_2Co_2TeO_6$, Phys. Rev. B **102**, 224429 (2020).

[17] H. Liu, J. c. v. Chaloupka, and G. Khaliullin, Kitaev Spin Liquid in 3*d* Transition Metal Compounds, Phys. Rev. Lett. **125**, 047201 (2020).

[18] L. Viciu, Q. Huang, E. Morosan, H. Zandbergen, N. Greenbaum, T. McQueen, and R. Cava, Structure and basic magnetic properties of the honeycomb lattice compounds $Na_2Co_2TeO_6$ and $Na_3Co_2SbO_6$, J. Solid State Chem. **180**, 1060 (2007).

[19] G. Xiao, Z. Xia, W. Zhang, X. Yue, S. Huang, X. Zhang, F. Yang, Y. Song, M. Wei, H. Deng, and D. Jiang, Crystal Growth and the Magnetic Properties of $Na_2Co_2TeO_6$ with Quasi-Two-Dimensional Honeycomb Lattice, Cryst. Growth Des. **19**, 2658 (2019).

[20] E. Lefrançois, M. Songvilay, J. Robert, G. Nataf, E. Jordan, L. Chaix, C. V. Colin, P. Lejay, A. Hadj-Azzem, R. Ballou, and V. Simonet, Magnetic properties of the honeycomb oxide $Na_2Co_2TeO_6$, Phys. Rev. B **94**, 214416 (2016).

[21] A. K. Bera, S. M. Yusuf, A. Kumar, and C. Ritter, Zigzag antiferromagnetic ground state with anisotropic correlation lengths in the quasi-two-dimensional honeycomb lattice compound $Na_2Co_2Teo_6$, Phys. Rev. B **95**, 094424 (2017).

[22] W. Chen, X. Li, Z. Hu, Z. Hu, L. Yue, R. Sutarto, F. He, K. Iida, K. Kamazawa, W. Yu, X. Lin, and Y. Li, Spin-orbit phase behavior of $Na_2Co_2TeO_6$ at low temperatures, Phys. Rev. B **103**, L180404 (2021).

[23] S. K. Pandey and J. Feng, Spin interaction and magnetism in cobaltate kitaev candidate materials: an *ab initio* and model hamiltonian approach, arXiv preprint arXiv:2205.03836 (2022).

[24] J. c. v. Chaloupka, G. Jackeli, and G. Khaliullin, Kitaev-Heisenberg Model on a Honeycomb Lattice: Possible Exotic Phases in Iridium Oxides A_2IrO_3, Phys. Rev. Lett. **105**, 027204 (2010).

[25] Y. Singh, S. Manni, J. Reuther, T. Berlijn, R. Thomale, W. Ku, S. Trebst, and P. Gegenwart, Relevance of the Heisenberg-Kitaev Model for the Honeycomb Lattice Iridates A_2IrO_3, Phys. Rev. Lett. **108**, 127203 (2012).

[26] Y. Singh and P. Gegenwart, Antiferromagnetic Mott insulating state in single crystals of the honeycomb lattice material Na_2IrO_3, Phys. Rev. B **82**, 064412 (2010).

[27] S. K. Choi, R. Coldea, A. N. Kolmogorov, T. Lancaster, I. I. Mazin, S. J. Blundell, P. G. Radaelli, Y. Singh, P. Gegenwart, K. R. Choi, S.-W. Cheong, P. J. Baker, C. Stock, and J. Taylor, Spin Waves and Revised Crystal Structure of Honeycomb Iridate Na_2IrO_3, Phys. Rev. Lett. **108**, 127204 (2012).

[28] A. Biffin, R. D. Johnson, S. Choi, F. Freund, S. Manni, A. Bombardi, P. Manuel, P. Gegenwart, and R. Coldea, Unconventional magnetic order on the hyperhoneycomb Kitaev lattice in $\beta-Li_2IrO_3$: Full solution via magnetic resonant x-ray diffraction, Phys. Rev. B **90**, 205116 (2014).

[29] A. Biffin, R. D. Johnson, I. Kimchi, R. Morris, A. Bombardi, J. G. Analytis, A. Vishwanath, and R. Coldea, Noncoplanar and Counterrotating Incommensurate Magnetic Order Stabilized by Kitaev Interactions in $\gamma-Li_2IrO_3$, Phys. Rev. Lett. **113**, 197201 (2014).

[30] B. H. Kim, G. Khaliullin, and B. I. Min, Electronic excitations in the edge-shared relativistic Mott insulator: Na_2IrO_3, Phys. Rev. B **89**, 081109 (2014).

[31] H. Gretarsson, J. P. Clancy, X. Liu, J. P. Hill, E. Bozin, Y. Singh, S. Manni, P. Gegenwart, J. Kim, A. H. Said, D. Casa, T. Gog, M. H. Upton, H.-S. Kim, J. Yu, V. M. Katukuri, L. Hozoi, J. van den Brink, and Y.-J. Kim, Crystal-Field Splitting and Correlation Effect on the Electronic Structure of A_2IrO_3, Phys. Rev. Lett. **110**, 076402 (2013).

[32] K. W. Plumb, J. P. Clancy, L. J. Sandilands, V. V. Shankar, Y. F. Hu, K. S. Burch, H.-Y. Kee, and Y.-J. Kim, $\alpha-RuCl_3$: A spin-orbit assisted Mott insulator on a honeycomb lattice, Phys. Rev. B **90**, 041112 (2014).

[33] R. D. Johnson, S. C. Williams, A. A. Haghighirad, J. Singleton, V. Zapf, P. Manuel, I. I. Mazin, Y. Li, H. O. Jeschke, R. Valentí, and R. Coldea, Monoclinic crystal structure of $\alpha-RuCl_3$ and the zigzag antiferromagnetic ground state, Phys. Rev. B **92**, 235119 (2015).

[34] A. Banerjee, C. A. Bridges, J.-Q. Yan, A. A. Aczel, L. Li, M. B. Stone, G. E. Granroth, M. D. Lumsden, Y. Yiu, J. Knolle, S. Bhattacharjee, D. L. Kovrizhin, R. Moessner, D. A. Tennant, D. G. Mandrus, and S. E. Nagler, Proximate Kitaev quantum spin liquid behaviour in a honeycomb magnet, Nat. Mat. **15**, 733 (2016).

[35] H.-S. Kim, V. S. V., A. Catuneanu, and H.-Y. Kee, Kitaev magnetism in honeycomb $RuCl_3$ with intermediate spin-orbit coupling, Phys. Rev. B **91**, 241110 (2015).

[36] W. Wang, Z.-Y. Dong, S.-L. Yu, and J.-X. Li, Theoretical investigation of magnetic dynamics in $\alpha-rucl_3$, Phys. Rev. B **96**, 115103 (2017).

[37] A. M. Cook, S. Matern, C. Hickey, A. A. Aczel, and A. Paramekanti, Spin-orbit coupled $j_{\rm eff} = 1/2$ iridium moments on the geometrically frustrated fcc lattice, Phys. Rev. B **92**, 020417 (2015).

[38] G. Cao, A. Subedi, S. Calder, J.-Q. Yan, J. Yi, Z. Gai, L. Poudel, D. J. Singh, M. D. Lumsden, A. D. Christianson, B. C. Sales, and D. Mandrus, Magnetism and electronic structure of la_2zniro_6 and la_2mgiro_6: Candidate $J_{\rm eff} = \frac{1}{2}$ mott insulators, Phys. Rev. B **87**, 155136 (2013).

[39] A. A. Aczel, A. M. Cook, T. J. Williams, S. Calder, A. D. Christianson, G.-X. Cao, D. Mandrus, Y.-B. Kim, and A. Paramekanti, Highly anisotropic exchange interactions of $j_{\rm eff} = \frac{1}{2}$ iridium moments on the fcc lattice in $la_2biro_6 (b = {\rm Mg}, {\rm Zn})$, Phys. Rev. B **93**, 214426 (2016).

[40] S. Kanungo, K. Mogare, B. Yan, M. Reehuis, A. Hoser, C. Felser, and M. Jansen, Weak orbital ordering of ir t_{2g} states in the double perovskite sr_2ceiro_6, Phys. Rev. B **93**, 245148 (2016).

[41] W. K. Zhu, C.-K. Lu, W. Tong, J. M. Wang, H. D. Zhou, and S. X. Zhang, Strong ferromagnetism induced by canted antiferromagnetic order in double perovskite iridates $(la_{1-x}sr_x)_2zniro_6$, Phys. Rev. B **91**, 144408 (2015).

[42] Y. Luo, C. Cao, B. Si, Y. Li, J. Bao, H. Guo, X. Yang, C. Shen, C. Feng, J. Dai, G. Cao, and Z.-a. Xu, Li_2RhO_3: A spin-glassy relativistic Mott insulator, Phys. Rev. B **87**, 161121 (2013).

[43] V. M. Katukuri, K. Roszeitis, V. Yushankhai, A. Mitrushchenkov, H. Stoll, M. van Veenendaal, P. Fulde, J. van den Brink, and L. Hozoi, Electronic structure of low-dimensional 4d5 oxides: Interplay of ligand distortions, overall lattice anisotropy, and spin–orbit interactions, Inorganic Chemistry **53**, 4833 (2014).

[44] T. Birol and K. Haule, $J_{\rm eff} = 1/2$ mott-insulating state in

rh and ir fluorides, Phys. Rev. Lett. **114**, 096403 (2015).
[45] J. F. Vente, J. K. Lear, and P. D. Battle, Sr4 –carho6: a magnetically ordered rh compound, J. Mater. Chem. **5**, 1785 (1995).
[46] S. Calder, L. Li, S. Okamoto, Y. Choi, R. Mukherjee, D. Haskel, and D. Mandrus, Spin-orbit driven magnetic insulating state with $J_{\text{eff}} = \frac{1}{2}$ character in a $4d$ oxide, Phys. Rev. B **92**, 180413 (2015).
[47] G. Kresse and D. Joubert, From ultrasoft pseudopotentials to the projector augmented-wave method, Phys. Rev. B **59**, 1758 (1999).
[48] P. E. Blöchl, Projector augmented-wave method, Phys. Rev. B **50**, 17953 (1994).
[49] G. Kresse and J. Furthmüller, Efficient iterative schemes for *ab initio* total-energy calculations using a plane-wave basis set, Phys. Rev. B **54**, 11169 (1996).
[50] J. P. Perdew, K. Burke, and M. Ernzerhof, Generalized gradient approximation made simple, Phys. Rev. Lett. **77**, 3865 (1996).
[51] A. I. Liechtenstein, V. I. Anisimov, and J. Zaanen, Density-functional theory and strong interactions: Orbital ordering in mott-hubbard insulators, Phys. Rev. B **52**, R5467 (1995).
[52] A. A. Mostofi, J. R. Yates, Y.-S. Lee, I. Souza, D. Vanderbilt, and N. Marzari, wannier90: A tool for obtaining maximally-localised wannier functions, Comput. Phys. Commun. **178**, 685 (2008).
[53] Q. Gu, Add onsite soc term to wannier90_hr, `https://github.com/qqgu/Wannier_Add_onsite_SOC/blob/master/tutorial.ipynb` (2020).
[54] S. M. Winter, Y. Li, H. O. Jeschke, and R. Valentí, Challenges in design of Kitaev materials: Magnetic interactions from competing energy scales, Phys. Rev. B **93**, 214431 (2016).
[55] G. Jha and T. Heine, DFTB Parameters for the Periodic Table: Part III, Spin-Orbit Coupling, Journal of Chemical Theory and Computation **18**, 4472 (2022), pMID: 35737969.
[56] S. L. Adler, Quantum theory of the dielectric constant in real solids, Phys. Rev. **126**, 413 (1962).
[57] N. Wiser, Dielectric constant with local field effects included, Phys. Rev. **129**, 62 (1963).
[58] F. Aryasetiawan, M. Imada, A. Georges, G. Kotliar, S. Biermann, and A. I. Lichtenstein, Frequency-dependent local interactions and low-energy effective models from electronic structure calculations, Phys. Rev. B **70**, 195104 (2004).
[59] I. Affleck and M. Oshikawa, Field-induced gap in cu benzoate and other $s = \frac{1}{2}$ antiferromagnetic chains, Phys. Rev. B **60**, 1038 (1999).
[60] S. Toth and B. Lake, Linear spin wave theory for single-q incommensurate magnetic structures, J. Phys.: Condens. Matter **27**, 166002 (2015).
[61] N. Ntallis, V. Borisov, Y. O. Kvashnin, D. Thonig, E. Sjöqvist, A. Bergman, A. Delin, O. Eriksson, and M. Pereiro, Connection between magnetic interactions and the spin-wave gap of the insulating phase of $naoso_3$, Phys. Rev. B **104**, 134433 (2021).
[62] J. Knolle, D. L. Kovrizhin, J. T. Chalker, and R. Moessner, Dynamics of a two-dimensional quantum spin liquid: Signatures of emergent majorana fermions and fluxes, Phys. Rev. Lett. **112**, 207203 (2014).